Chinese Physics Letters

LETTER

Flow-Reversal Hydrodynamic Metamaterial

Cite as: Junjie Xiao *et al*. 2026 *Chin. Phys. Lett.* **43** 100801

DOI CSTR

Recommended Articles

Modeling Bacterial Flow Field with Regularized Singularities
Yaochen Yang, Daiki Matsunaga, Da Wei, and Fanlong Meng
Chin. Phys. Lett. **43**, 050901 (2026)

AI-Driven Acoustic Metamaterials for Pixel-Accurate Sound Insulation Control
Kaijing Liu, Yihuan Zhu, Jiachen Meng, Ruizhi Dong, Xu Wang, and Yong Li
Chin. Phys. Lett. **43**, 021001 (2026)

First Full-Scale Field Experiments: Topologically Amplified Seismic Surface Waves via Interface States in a 1D Metamaterial
Xin-Chao Zhang, Ning Zheng, Chang-Yin Ji, Yu-Lin Lu, and Qing-Fan Shi
Chin. Phys. Lett. **42**, 120603 (2025)

Addressing the Ultra-Central Puzzle with Initial-State Nuclear Structures
Qi Wang, Long-Gang Pang, and Xin-Nian Wang
Chin. Phys. Lett. **43**, 020101 (2026)

A series journal of Chinese Physical Society distributed by IOP Publishing

Chinese Physics Letters

Chin. Phys. Lett. **43** 100801 (2026)

LETTER

DOI: 10.1088/0256-307X/43/10/100801
CSTR: 32039.14.0256-307X.43.10.100801

Flow-Reversal Hydrodynamic Metamaterial

Junjie Xiao(肖俊杰)[1], Zihan Qian(钱梓涵)[1], Yanting Xu(徐燕婷)[1], Qiao Chen(陈桥)[1], Sixu Chen(陈思旭)[1], and Mengyao Chen(陈梦瑶)[1,2,*]

[1]School of Engineering, South China Agricultural University, Guangzhou 510642, China
[2]Shenzhen Institutes of Advanced Technology (SIAT), Chinese Academy of Sciences (CAS), Shenzhen 518055, China

[*]Corresponding author. Email: mychen@scau.edu.cn

In passive viscous systems, the local flow field is governed by the prescribed hydraulic properties and the applied pressure boundary conditions. Hydrodynamic metamaterials based on spatially engineered permeability or viscosity distributions can redistribute, concentrate, conceal, and even redirect flow fields. Transformation-based rotators can, in principle, produce large rotations of the local velocity direction; however, such transport states are encoded in the prescribed material architecture and generally require increasingly strong anisotropy as the rotation angle increases. This motivates an alternative strategy for achieving dynamically tunable localized reverse transport without redesigning the passive structure. Here, we demonstrate a flow-reversal hydrodynamic metamaterial that creates a target region with velocity opposite to the imposed background flow while retaining an approximately uniform external flow. The device combines an inner annular array of active source–sink dipoles with a surrounding passive Hele–Shaw compensation shell. The active dipoles supply the hydraulic work required to overcome the background transport within the target region, whereas the passive shell suppresses the exterior disturbance by hydraulic-resistance matching. This active–passive coupled design enables complete internal flow reversal while maintaining an almost undisturbed external flow field. This work uses active transport control on hydrodynamic metamaterials, enabling programmable localized transport in pressure-driven viscous flows.

Introduction

The ability to manipulate fluid transport with high spatial precision is of fundamental importance in a wide range of scientific and engineering applications, including microfluidics, thermal management, soft robotics, chemical processing, and biological systems. In recent years, hydrodynamic metamaterials [1−5] have emerged as a powerful platform for tailoring viscous flow fields through the rational design of effective transport properties [6]. Inspired by transformation mapping theory [7−11] and scattering cancellation theory [12−14], these artificial fluidic media enable unprecedented control over streamline distributions by spatially engineering permeability or hydraulic conductivity. A variety of functionalities have been demonstrated, including hydrodynamic cloaking [15−18], shielding [19−21], concentration [22,23], rotation [23,24], expansion [25], and camouflage [26], providing new opportunities for manipulating fluid transport beyond conventional geometric approaches.

Most existing hydrodynamic metamaterials are passive, relying on spatial modulation of hydraulic resistance under Darcy-type transport laws, where velocity is proportional to the local pressure gradient: $\boldsymbol{u} = -k\nabla p$, with $k > 0$. This positive-definite relation dictates that velocity always points from high to low pressure, making transport direction reversal challenging. Transformation-based hydrodynamic metamaterials can redirect local flow fields through spatially engineered anisotropic transport properties [24]. In principle, transformation rotators can prescribe large rotation angles, including a nominal 180° rotation of the velocity field. However, increasing the rotation angle generally requires increasingly strong anisotropy of the effective transport tensor, while the prescribed rotation is encoded in the material architecture. This motivates an alternative strategy in which localized reverse transport is generated actively and can be tuned without redesigning the passive medium.

Achieving localized flow reversal under an otherwise unchanged background driving condition would provide an additional degree of freedom for controlling transport in pressure-driven flows. In particular, the ability to independently regulate the transport direction within a prescribed region could enable localized upstream transport, reconfigurable flow pathways, and particle manipulation without reversing the overall background flow. Such functionality would extend conventional passive hydrodynamic metamaterial approaches, which primarily rely on spatial modulation of hydraulic properties, toward active control of local transport.Thus, localized flow reversal unlocks new capabilities in microfluidics, fluidic logic, and adaptive transport systems. However, realizing a flow-reversal metamaterial remains highly challenging because it requires overcoming the dissipative nature of viscous flow while simultaneously maintaining compatibility with the surrounding flow field.

Recent studies have shown that active flow manipulation can be achieved through externally driven source–sink elements [27−29], which locally reshape the flow field. In particular, hydrodynamic dipoles [30] formed by paired injection and extraction ports provide a convenient mechanism for generating controllable flow patterns while preserving global mass conservation. These active elements [31−33] have been employed to enhance mixing and manipulate particles. Through linear superposition, distributed dipoles can reconstruct programmable velocity fields that are inaccessible in passive systems. These characteristics make fluidic dipoles an ideal building block for extending hydrodynamic metamaterials from passive permeability engineering to active transport control.

Here we present a flow-reversal hydrodynamic metamaterial that generates localized upstream transport in a pressure-driven Hele–Shaw flow while maintaining an almost undisturbed background field. The proposed design combines distributed source–sink actuation with passive hydraulic compensation to independently control the target-region transport and the exterior flow disturbance. The resulting flow-reversal state is established theoretically, evaluated through numerical simulations, and validated experimentally. These results demonstrate that active hydraulic actuation can extend hydrodynamic metamaterials beyond passive streamline redistribution and enable programmable control of transport direction in low-Reynolds-number flows.

Received 23 July 2026; accepted 4 September 2026; published 30 September 2026
© 2026 Chinese Physical Society and IOP Publishing Ltd. All rights, including for text and data mining, AI training, and similar technologies, are reserved.

Check for updates

Theoretical Design

Passive Hele–Shaw Constraint

The device operates in a shallow cell of local gap height $h(x,y)$. Under the lubrication approximation and at low Reynolds number, the depth-averaged velocity $\boldsymbol{u}$ and the depth-integrated planar flux $\boldsymbol{q}$ are

$$\boldsymbol{u} = -\frac{h^2}{12\mu}\nabla p, \quad \boldsymbol{q} = h\boldsymbol{u} = -\frac{h^3}{12\mu}\nabla p, \tag{1}$$

where p is pressure and μ is dynamic viscosity. Mass conservation gives

$$\nabla \cdot \boldsymbol{q} = s, \tag{2}$$

where s is the local source density. In the source-free part of a constant-gap cell, this reduces to $\nabla^2 p = 0$. In the variable-gap compensation shell, however, the governing equation is

$$\nabla \cdot (h^3 \nabla p) = 0. \tag{3}$$

This distinction is essential: the passive shell is realized by a spatially varying gap height and therefore cannot be modeled as a uniform gap Laplace problem.

For a uniform background region of height h_b, a far-field pressure gradient ∇p_∞ produces the background velocity

$$\boldsymbol{u}_\mathrm{b} = -\frac{h_\mathrm{b}^2}{12\mu}\nabla p_\infty = U_0 \boldsymbol{e}_x, \tag{4}$$

where the hydraulic mobility $h^2/12\mu$ remains strictly positive for passive flows because both the gap height and the fluid viscosity are positive. Therefore, under an unchanged far-field pressure gradient, the velocity is always directed from high pressure toward low pressure. Spatial modulation of the gap height, or equivalently the hydraulic permeability, can redistribute the velocity magnitude and streamline patterns, but cannot reverse the transport direction. Consequently, existing passive hydrodynamic metamaterials, including cloaks, concentrators and rotators, remain constrained by the same transport direction imposed by Darcy's law. Achieving sustained local flow reversal therefore requires external hydraulic work, which cannot be provided by passive permeability engineering alone.

Active Source–Sink Dipoles

The active layer consists of paired injection and extraction ports. A dipole contains a source and a sink with equal volumetric flow-rate magnitude Q_i, separated by a vector d_i. Thus, each pair preserves global mass balance even though it injects hydraulic work locally. Away from the finite-sized ports, the leading-order depth-averaged potential of a single dipole may be written as

$$\phi_i(\boldsymbol{r}) = \frac{\mathcal{M}_i}{2\pi r}\cos(\theta - \theta_i), \quad \mathcal{M}_i = \frac{Q_i d_i}{h_\mathrm{a}}, \tag{5}$$

where h_a is the local active layer height, $d_i = |\boldsymbol{d}_i|$, and θ_i specifies the dipole orientation. The associated velocity correction is $\boldsymbol{u}_i = \nabla\phi_i$ and decays as r^{-2} in the far field. The finite-port problem used in the numerical model is more accurate than this point-dipole approximation, and the expression above is used only to clarify the symmetry and superposition principle.

At low Reynolds number, the active correction from a finite set of dipoles is linear to leading order. The depth-averaged velocity can therefore be represented as

$$\boldsymbol{u} = \boldsymbol{u}_\mathrm{b} + \sum_{i=1}^{N} \boldsymbol{u}_i + \boldsymbol{u}_\mathrm{p}, \tag{6}$$

where $\boldsymbol{u}_\mathrm{p}$ is the velocity correction associated with the passive compensation shell. For a background flow along $+x$, the dipole orientations and strengths are selected to approximate the first angular harmonic of the required correction around the target region. In practice, the discrete values Q_i and θ_i are determined by numerical optimization under the constraint $\sum_i Q_i = 0$.

Active–Passive Design Objective

In our design, the structure of the metamaterial comprises four domains: a circular target region Ω_T of radius R_1 ($r < R_1$), an annular active layer containing the source–sink dipoles ($R_2 > r > R_1$), a surrounding passive compensation shell extending to R_3 ($R_3 > r > R_2$), and the uniform background region ($r > R_3$). The active layer is designed to create a negative target-region mean velocity relative to the imposed background direction. Here, we define the reversal metric

$$\mathcal{R} = -\frac{\langle u_x \rangle_{\Omega_\mathrm{T}}}{U_0}, \tag{7}$$

where $\langle\cdot\rangle_{\Omega_\mathrm{T}}$ denotes the area average over the target region. Here, localized flow reversal is defined by a change in sign of the net streamwise velocity within the target region relative to the background flow direction; it does not require individual fluid elements to follow a closed recirculation path. A reversed state requires $\mathcal{R} > 0$. The corresponding exterior-field error is quantified by

$$\mathcal{E}_\mathrm{out} = \frac{\|\boldsymbol{u} - \boldsymbol{u}_\mathrm{b}\|_{L^2(\Omega_\mathrm{out})}}{\|\boldsymbol{u}_\mathrm{b}\|_{L^2(\Omega_\mathrm{out})}}, \tag{8}$$

where Ω_out is a specified exterior observation domain. The design problem is therefore not simply to maximize reverse flow. It is to achieve $\mathcal{R} > 0$ while minimizing $\mathcal{E}_\mathrm{out}$. The outer layer is passive and is implemented through a designed gap-height profile $h_\mathrm{p}(r,\theta)$. Its role is to redistribute the pressure and flux perturbations generated by the active ports so that the exterior field approaches the original background state. In the idealized limit,

$$\boldsymbol{u}_\mathrm{act} + \boldsymbol{u}_\mathrm{p} \to 0 \text{ in } \Omega_\mathrm{out}, \tag{9}$$

whereas the active correction dominates inside Ω_T. This is the active–passive separation of functions: the dipoles produce reversal, while the shell reduces exterior disturbance. This functional separation provides a means of independently regulating the local transport direction and the exterior flow response, thereby decoupling target-region transport from far-field compatibility.

The device architecture is illustrated schematically in Fig. 1(a), while the corresponding simulated velocity and pressure fields are presented in Figs. 1(b) and 1(c), respectively. The parametric simulations demonstrate that localized upstream transport is established inside the target region while leaving the surrounding flow nearly undisturbed. The underlying transport mechanism is further elucidated by the pressure and velocity profiles shown in Figs. 1(d) and 1(e). The pressure profile exhibits opposite monotonic gradients inside and outside the target region, consistent with the transition from the background pressure-driven flow to the localized reverse-flow state. Correspondingly, the streamwise velocity becomes negative only within the target region and gradually recovers to the imposed background value outside the metamaterial. Quantitatively, the flow-reversal metric reaches $\mathcal{R} \approx 1.30$, while the exterior-flow error is $\mathcal{E}_\mathrm{out} \approx 0$, confirming complete localized flow reversal with negligible disturbance to the surrounding flow.

Simulation

To validate the proposed flow-reversal hydrodynamic metamaterial, three-dimensional numerical simulations were performed using COMSOL Multiphysics by solving the incompressible Stokes flow equations under steady, low-Reynolds-number conditions. The computational domain was a 40 mm × 40 mm × 1 mm Hele–Shaw channel, and the laminar flow interface was employed. A concentric metamaterial was positioned at the center of the channel and consisted of four functional regions: a central target region, an active dipole layer, a passive Hele–Shaw compensation layer, and the surrounding background region. The target region had a radius of $R_1 = 5$ mm, while the active dipole layer and passive compensation layer extended to $R_2 = 7.5$ mm and $R_3 = 10$ mm, respectively. A uniform pressure-driven background flow was generated by imposing a constant pressure difference between the inlet and outlet boundaries, producing an approximately uniform far-field velocity $U_0\boldsymbol{e}_x$. No-slip boundary condi-

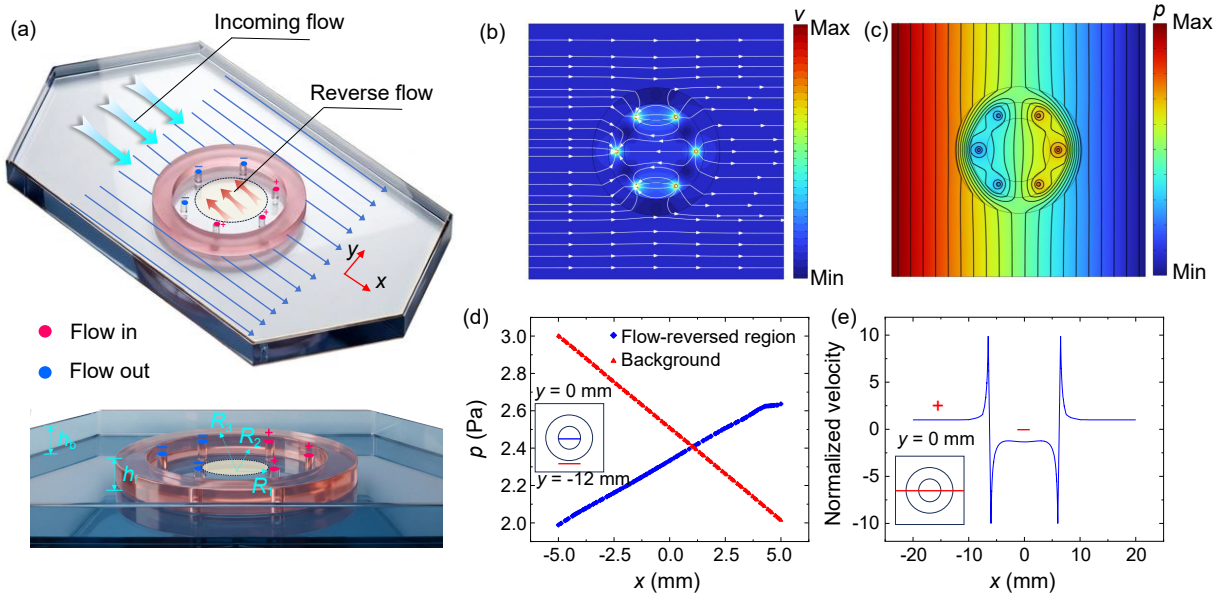

Fig. 1. Design principle and parametric simulation results. (a) Schematic of the flow-reversal hydrodynamic metamaterial: an active annular source–sink layer produces the target flow reversal and a passive depth-modulated shell reduces the exterior disturbance. (b) Simulated velocity magnitude and streamlines. (c) The corresponding simulated pressure field. (d) Pressure profiles inside the target region and background regions along the observation lines $y = 0$ mm and $y = -12$ mm. (e) Normalized streamwise velocity along the observation line $y = 0$ mm.

tions were imposed on the top and bottom plates, while symmetry boundary conditions were applied along the lateral boundaries.

The active dipole layer consisted of six circular ports uniformly distributed along the annular ring ($R_2 > r > R_1$). The ports had an inner diameter of 0.75 mm and were equally spaced with alternating functions, comprising three injection ports and three extraction ports. Equal volumetric flow rates were imposed at the three injection and three extraction ports to ensure zero net mass flux while generating a localized active flow field. Outside the active layer, the gap height of the passive Hele–Shaw compensation layer was optimized to be 0.62 mm by minimizing the far-field velocity error while maintaining complete flow reversal inside the target region.

Figures 2(c) and 2(d) compare the simulated flow fields with and without active actuation while maintaining the same passive compensation layer. When the six active ports are turned off, the target region follows the imposed background flow and no flow reversal is observed. Although the passive compensation layer modifies the local hydraulic resistance, it cannot generate upstream transport because no external hydraulic work is supplied. Consequently, the background streamlines are slightly distorted owing to the mismatch between the compensation layer and the surrounding Hele–Shaw channel [Fig. 2(d)]. When the six active ports are turned on, the streamlines outside the metamaterial recover an almost uniform and parallel configuration, whereas the velocity inside the target region is completely reversed with respect to the imposed background flow [Fig. 2(c)]. Because the passive shell redistributes the hydraulic resistance, compensating for the disturbance introduced by the active source–sink array, it is worth noting that the passive shell counteracts the perturbations imposed by the active source–sink array on the corresponding background flow. Therefore, when the background flow varies, the design performance can be maintained by adjusting the volumetric flow rate of the dipoles according to the background inflow velocity. These results demonstrate that the proposed active–passive architecture simultaneously achieves local transport reversal while maintaining the undisturbed background flow field.

Experimental Realization

To experimentally validate the proposed flow-reversal hydrodynamic metamaterial, a macroscopic prototype was fabricated according to the numerical model design [Figs. 2(a) and 2(b)]. The Hele–Shaw channel measured 40 mm × 40 mm with a uniform gap of 1.0 mm. The target region had a radius of $R_1 = 5.0$ mm, while the active dipole layer and passive compensation layer extended to $R_2 = 7.5$ mm and $R_3 = 10.0$ mm, respectively. The active layer consisted of six uniformly distributed circular ports with an inner diameter of 1.5 mm, comprising three injection ports and three extraction ports arranged alternately around the annulus. The device was fabricated using a BMF microArch® S150 micro-stereolithography system with HTL UV-curable photopolymer resin and subsequently assembled into a Hele–Shaw cell. The background flow was generated by a syringe pump at a constant flow rate of 3.00 mL/min, while the active dipole array was actuated by prescribing identical volumetric flow rates of 2.79 mL/min at each injection and extraction port, with opposite flow directions to maintain global mass conservation. Deionized water seeded with 50 µm polystyrene tracer particles was used as the working fluid. Particle motions were recorded using a high-speed camera operating at 60 fps, and particle trajectories were recorded from the top view and analyzed using particle-tracking velocimetry (PTV) to obtain the in-plane velocity components. PTV measurements were performed only after the pump flow rates and the observed flow pattern had stabilized. Because the out-of-plane positions of individual particles were not resolved, the measured particle velocities are not interpreted as direct measurements of the depth-averaged velocity. Under the Hele–Shaw approximation, the unresolved depth position primarily affects the measured velocity magnitude through the parabolic velocity profile, while preserving the sign of the in-plane velocity.

The experimentally measured flow fields are compared with the simulation results in Figs. 2(e)–2(h). To elucidate the role of the active source–sink array, two operating conditions were examined: passive compensation only and active–passive coupled operation. When the active source–sink array was turned off [Fig. 2(f)], the streamlines remained aligned with the imposed background flow throughout the target region, indicating that no flow reversal occurred (see experimental video S1 for details). As the flow passed through the passive compensation layer, the streamlines were deflected toward the annular region owing to the locally reduced hydraulic permeability. This disturbance persisted downstream of the device, where the streamlines remained noticeably curved and failed to recover the original parallel background flow, demonstrating that passive permeability modulation alone cannot simultaneously preserve the external flow field and reverse the local transport.

After activating the six-port source–sink array [Fig. 2(e)], the flow

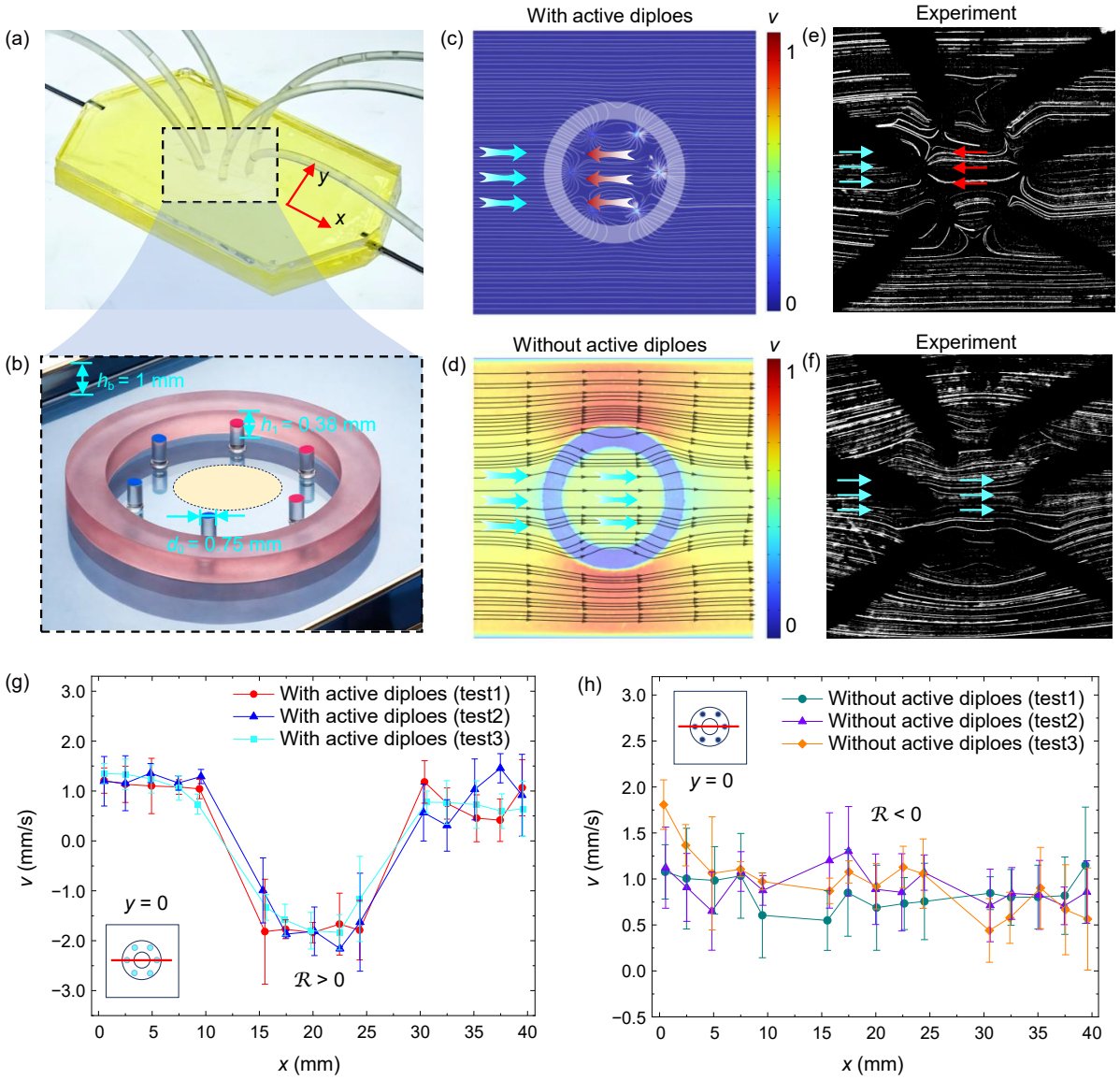

Fig. 2. Structure design and experimental realization of the flow-reversal hydrodynamic metamaterial. (a) The 3D-printed experimental setup. (b) The structure parameters showing the background gap h_b, active annulus, passive shell, port positions, and radii. (c) Simulated velocity field for the flow-reversal hydrodynamic metamaterial. (d) Simulated velocity field of the passive compensation only. (e) The experimental streamlines for the case with active dipoles. (f) The experimental streamlines for the case without active dipoles (see experimental video S1 for details). (g) The velocity distribution along the observation line ($y = 0$) for the case with active dipoles. (h) The velocity distribution along the observation line ($y = 0$) for the case without active dipoles.

topology changed markedly. The streamlines entering the device exhibited only slight deflection and rapidly recovered to straight, parallel trajectories after leaving the compensation layer, indicating that the far-field disturbance was effectively suppressed. In contrast, the flow inside the target region reversed completely, with the local streamlines oriented opposite to the imposed background flow (see experimental video S1 for details). These observations demonstrate that the active source–sink array generates the localized reverse transport, whereas the passive compensation layer cancels the disturbance introduced by the active actuation, thereby spatially decoupling the internal reverse flow from the surrounding pressure-driven transport.

The experimental observations agree closely with the numerical simulations. As shown in Fig. 2(g), the measured centerline velocity profiles exhibit a clear sign reversal within the target region while converging to the same background velocity outside the metamaterial. The corresponding quantitative metrics yield $\mathcal{R} \approx 1.67$ and $\mathcal{E}_{\text{out}} \approx 0.10$ for the active–passive configuration, confirming complete flow reversal with minimal background disturbance. In contrast, the passive-only configuration gives $\mathcal{R} \approx -0.58$ and $\mathcal{E}_{\text{out}} \approx 0.8$, indicating that no reverse transport is generated and that the surrounding flow remains strongly disturbed. The close agreement between simulations and experiments validates the proposed active–passive coupling mechanism.

In the present experiments, the injection and extraction branches were independently driven, with equal volumetric flow rate magnitudes prescribed at the source and sink ports. Alternatively, the extraction and injection branches can be hydraulically connected to form a closed recirculation loop. These two implementations impose equivalent source–sink boundary conditions on the internal flow field when the corresponding flow rates are matched.

Discussion

Having established the feasibility of the proposed flow-reversal metamaterial, we next examine the influence of the source–sink configuration on the reconstructed flow field. The theoretical model assumes a continuous annular distribution of hydraulic actuation surrounding the target region, whereas the practical implementation replaces it with a finite number of discrete source–sink ports. Consequently, the quality of the reconstructed reverse-flow field depends on how accurately the discrete actuation approximates the continuous

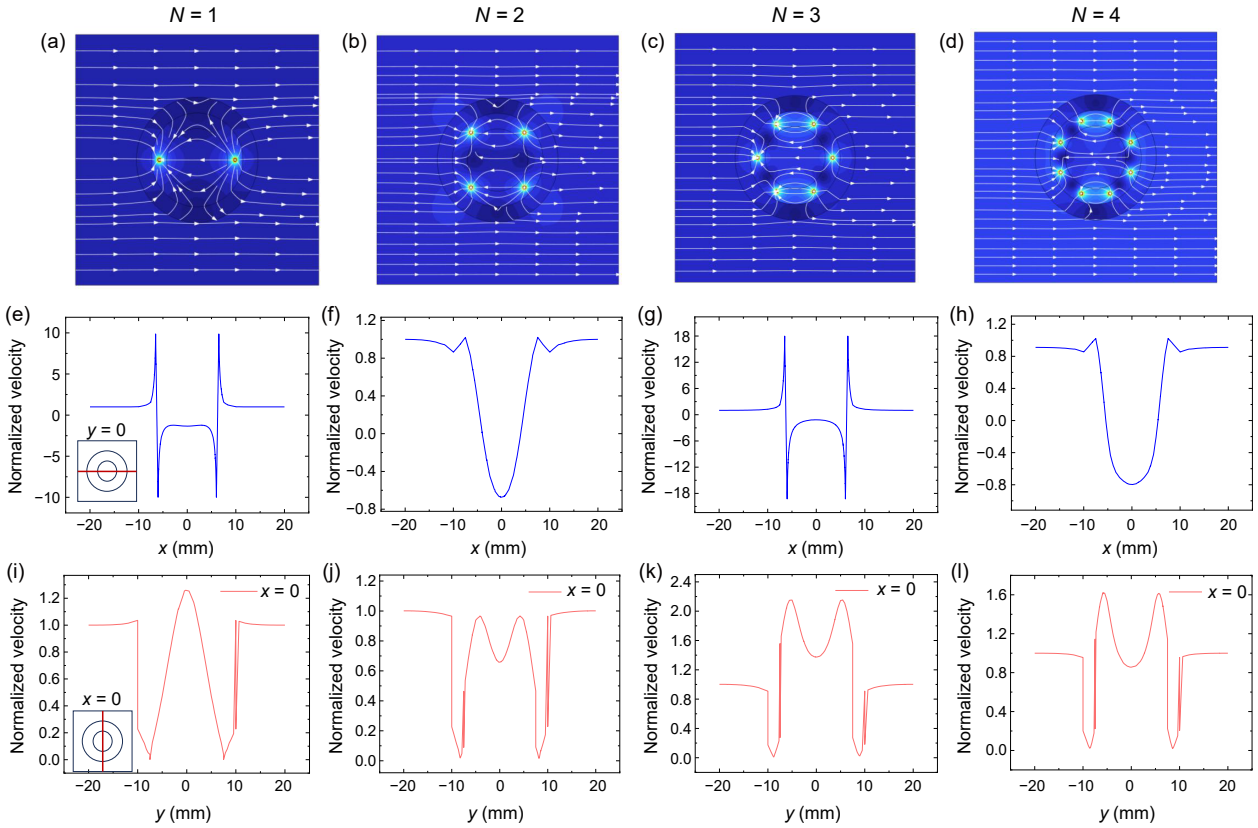

Fig. 3. The effect of the number of dipoles on the velocity fields. (a)–(d) Simulated velocity fields for the indicated numbers of dipoles, with identical total dipole moment and identical passive-shell geometry. (e)–(h) Normalized velocity profile along the observation line $y = 0$. (i)–(l) The normalized velocity profile along the observation line $x = 0$.

distribution.

As shown in Fig. 3, increasing the number of source–sink pairs progressively improves the uniformity of the reverse-flow region. When only a few ports are employed, the discrete nature of the actuation produces pronounced azimuthal variations in the velocity field, resulting in non-uniform reverse transport within the target region [Figs. 3(a)–3(d)]. These variations are also reflected in the velocity profiles measured along the horizontal [Figs. 3(e)–3(h)] and vertical centerlines [Figs. 3(i)–3(l)], where configurations with fewer ports exhibit significant velocity fluctuations. As the number of ports increases, these fluctuations are gradually suppressed and the velocity distribution approaches the nearly uniform profile predicted by the continuous theoretical model.

However, increasing the number of ports does not necessarily lead to a better practical design. Although additional source–sink elements improve flow uniformity, they also increase fabrication complexity, hydraulic interconnections, and the synchronization requirements of the pumping system. The design therefore involves a trade-off between hydraulic performance and experimental implementation. In the present work, three injection ports and three extraction ports provide a favorable compromise, producing a nearly uniform reverse-flow region while maintaining a simple and experimentally accessible architecture. More importantly, these results demonstrate that the continuous annular actuation assumed in the theoretical model can be accurately approximated using only a small number of properly distributed discrete source–sink elements, eliminating the need for a physically continuous actuator.

The central physical mechanism revealed by the present study is the decoupling of local transport from the far-field flow through active–passive coupling. The active source–sink field supplies the hydraulic work required to reverse the local velocity, whereas the passive compensation layer redistributes the hydraulic resistance to suppress the resulting exterior disturbance. These two functions are physically distinct but operate cooperatively: the active layer controls the transport direction inside the target region, while the passive layer restores the surrounding pressure-driven flow. Consequently, localized upstream transport can be embedded within an otherwise unidirectional flow without reversing the imposed far-field pressure gradient. Such a separation between local and far-field transport cannot be achieved by passive Darcy systems, in which both the velocity direction and the associated field redistribution are constrained by a positive-definite hydraulic mobility. The significance of the present work therefore lies not in global flow reversal, which can be trivially produced by reversing the applied pressure gradient, but in establishing a new transport mechanism that independently controls local transport direction and far-field compatibility.

It is useful to distinguish the present mechanism from transformation-based hydrodynamic rotators. A transformation rotator can, in principle, prescribe a large rotation of the local velocity field, including a nominal 180° rotation, through an appropriately designed anisotropic transport tensor. Such a state is therefore not fundamentally prohibited in a passive transformation framework. However, the required anisotropy becomes increasingly demanding as the prescribed rotation angle increases, and the rotation angle is intrinsically encoded in the spatial distribution of the effective transport properties. Consequently, changing the target transport state generally requires redesigning the metamaterial architecture. In the present system, by contrast, the reverse transport is generated by active source–sink forcing rather than by encoding a 180° rotation into the passive transport tensor. The passive layer instead serves to compensate for the exterior disturbance. This separation enables the target-region velocity to be tuned continuously through the source–sink strength while retaining the same passive structure and approximately preserving the far-field flow.

Although demonstrated here in a Hele–Shaw cell, the underlying design principle is not restricted to this specific configuration. Any pressure-driven transport system in which localized hydraulic actuation can be combined with passive regulation of the surrounding flow

field should, in principle, support the same active–passive coupling mechanism. This concept may therefore be extended to porous-media transport, electro-osmotic flows, and actively controlled microfluidic networks, providing a general framework for programmable transport in viscous-flow systems.

Conclusion

In this work, we have demonstrated an active–passive hydrodynamic metamaterial that realizes localized flow reversal in a pressure-driven Hele–Shaw flow. By integrating a six-port source–sink array with a passive Hele–Shaw compensation layer, the proposed design simultaneously achieves complete flow reversal inside a target region while preserving an almost undisturbed background flow. Theoretical analysis, numerical simulations, and experimental measurements consistently validate the proposed mechanism. More importantly, the present results demonstrate that active source–sink actuation and passive hydraulic compensation can decouple local transport from the far-field flow response. This active–passive mechanism extends hydrodynamic metamaterials beyond passive permeability engineering and provides a general route for realizing transport states that are inaccessible in passive Darcy systems.

Author Declarations

Authors M. C., J. X., and Z. Q. have filed a China provisional-patent application (No. 2026113289154) based on the structure design in this work. The other authors declare no competing interests.

Acknowledgements

This work was supported by the National Natural Science Foundation of China (Grant No. 1250040694), the Guangdong Basic and Applied Basic Research Foundation (Grant No. 2023A1515110651), and the Shenzhen Science and Technology Innovation Committee (Grant No. JCYJ20250604183050065).

References

[1] Chen M, Shen X, and Xu L 2023 *Droplet* **2** e79
[2] Morton K J, Loutherback K, Inglis D W, Tsui O K, Sturm J C, Chou S Y, and Austin R H 2008 *Proc. Natl. Acad. Sci. U.S.A.* **105** 7434
[3] Urzhumov Y A and Smith D R 2012 *Phys. Rev. E* **86** 056313
[4] Culver D and Urzhumov Y 2017 *Phys. Rev. E* **96** 063107
[5] Yang F, Zhang Z, Xu L, Liu Z, Jin P, Zhuang P, Lei M, Liu J, Jiang J H, Ouyang X, Marchesoni F, and Huang J 2024 *Rev. Mod. Phys.* **96** 015002
[6] Liu Z, Jin P, Lei M, Wang C, Zhuang P, Tan P, Jiang J H, Marchesoni F, and Huang J 2025 *Chem. Rev.* **125** 8655
[7] Pendry J B, Schurig D, and Smith D R 2006 *Science* **312** 1780
[8] Schurig D, Mock J J, Justice B J, Cummer S A, Pendry J B, Starr A F, and Smith D R 2006 *Science* **314** 977
[9] Chen M, Shen X, Chen Z, Lo J H Y, Liu Y, Xu X, Wu Y, and Xu L 2022 *Proc. Natl. Acad. Sci. U.S.A.* **119** e2207630119
[10] Chen M, Shen X, and Xu L 2024 *Appl. Phys. Lett.* **125** 171701
[11] Liu Z, Jin P, Lei M, Wang C, Marchesoni F, Jiang J H, and Huang J 2024 *Nat. Rev. Phys.* **6** 554
[12] Gömöry F, Solovyov M, Šouc J, Navau C, Prat-Camps J, and Sanchez A 2012 *Science* **335** 1466
[13] Han T, Bai X, Gao D, Thong J T L, Li B, and Qiu C W 2014 *Phys. Rev. Lett.* **112** 054302
[14] Han T, Ye H, Luo Y, Yeo S P, Teng J, Zhang S, and Qiu C W 2014 *Adv. Mater.* **26** 3478
[15] Park J, Youn J R, and Song Y S 2019 *Phys. Rev. Lett.* **123** 074502
[16] Chen M, Shen X, and Xu L 2022 *Innovation* **3** 100263
[17] Zhang L, Zhang Y, Liu J, Yang F, Jin P, and Huang J 2026 *Adv. Mater.* **38** e73690
[18] Li Y, Zhou Y, Wang Y, Jiang W, Yang F, Jin P, and Huang J 2026 *Adv. Mater.* **38** e19721
[19] Boyko E, Bacheva V, Eigenbrod M, Paratore F, Gat A D, Hardt S, and Bercovici M 2021 *Phys. Rev. Lett.* **126** 184502
[20] Ren F, Wang C, and Tang H 2021 *Phys. Fluids* **33** 093602
[21] Boyadjian O, Boulais E, and Gervais T 2022 *Phys. Rev. Appl.* **17** 014012
[22] Park J, Youn J R, and Song Y S 2021 *Extreme Mech. Lett.* **42** 101061
[23] Hu E, Wang B, and Wang X 2026 *Mater. Horiz.* **13** 8011
[24] Park J, Youn J R, and Song Y S 2019 *Phys. Rev. Appl.* **12** 061002
[25] Chen M, Shen X, Zhu G, and Li B 2024 *Phys. Fluids* **36** 053611
[26] Yang F, Zhou Y, Jin P, Liu J, Li Z, Zhang L, Dai G, Xu L, and Huang J 2026 *Phys. Rev. Fluids* **11** 064101
[27] Crane L J and McVeigh A G 2011 *Z. angew. Math. Mech.* **91** 681
[28] Yao N Z, Wang B, Wang H, Wu C L, and Wang X 2024 *Phys. Fluids* **36** 094126
[29] Jiang C, Nie H, Chen M, Shen X, and Xu L 2025 *Adv. Mater.* **37** 2313986
[30] Głódkowski A, Peña-Benítez F, and Surówka P 2023 *Phys. Rev. E* **107** 034142
[31] Qasaimeh M A, Gervais T, and Juncker D 2011 *Nat. Commun.* **2** 464
[32] Goyette P A, Boulais É, Normandeau F, Laberge G, Juncker D, and Gervais T 2019 *Nat. Commun.* **10** 1781
[33] Ali D S, Glia A, Sukumar P, Deliorman M, and Qasaimeh M A 2025 *Sci. Rep.* **15** 2252